Numerical Simulation of Thin Film Breakup on Nonwettable Surfaces

IOP Conf. Series: Journal of Physics: Conf. Series **796** (2017) 012038 doi:10.1088/1742-6596/796/1/012038

Numerical Simulation of Thin Film Breakup on Nonwettable Surfaces

Nicola Suzzi[1] **and Giulio Croce**[1]

[1]DPIA - Dipartimento Politecnico di Ingegneria e Architettura - Universitá di Udine - Via delle Scienze - 33100 - Udine (UD) - Italy

E-mail: giulio.croce@uniud.it

Abstract. When a continuous film flows on a *nonwettable* substrate surface, it may break up, with the consequent formation of a dry-patch. The actual shape of the resulting water layer is of great interest in several engineering applications, from in-flight icing simulation to finned dehumidifier behavior modeling. Here, a 2D numerical solver for the prediction of film flow behavior is presented. The effect of the contact line is introduced via the disjoining pressure terms, and both gravity and shear are included in the formulation.
The code is validated with literature experimental data for the case of a stationary dry-patch on an inclined plane. Detailed numerical results are compared with literature simplified model prediction. Numerical simulation are then performed in order to predict the threshold value of the film thickness allowing for film breakup and to analyze the dependence of the dynamic contact angle on film velocity and position along the contact line. Those informations will be useful in order to efficiently predict more complex configuration involving multiple breakups on arbitrarily curved substrate surfaces (as those involved in in-flight icing phenomena on aircraft).

1. Introduction

A thin layer of liquid can spread over a solid substrate as a collection of tiny droplets, as an ensemble of rivulets or as a continuous film. The details of this transitions have an impact on different engineering problems: as an example, in-flight icing phenomenon on aircraft surface is driven by the evolution of the water layer fed by a stream of super-cooled droplets from the cloud; depending on the cloud water content and the fluid flow field and temperature, the liquid layer may take one of the above mentioned forms and influence the consequent ice accretion and its effect on aircraft aerodynamics. Also fogging and defogging of a car windshield or heat transfer on dehumidifier fin surfaces are affected by condensation and evaporation phenomena with droplets growth, coalescence and motion over solid substrates.

The early studies reported in open literature followed an analytical/integral approach: a first paper by Hartley and Murgatroyd [1] considered the separation of a laminar film flowing vertically under gravity, proposing a critical breakup threshold for the liquid flow rate based on a force balance at the apex of the dry-patch. In [2], the authors modeled the transition between still droplets and moving ones via a Lagrangian approach, simulating the process of birth, growth, coalescence of the individual droplets and detecting their motion by a force balance. A different approach is the straightforward numerical solution of the two dimensional lubrication equation. Witelski and Bowen [3] proposed an efficient implicit scheme for the numerical integration of the lubrication equation, via an ADI factorization. The authors considered only fully wetted surfaces.

Schwartz and Eley [4] introduced the disjoining pressure term in order to model the substrate wettability and the development of dry-patches. The disjoining pressure definition was adjusted to match the static contact angle. The modeling of the contact angle via disjoining pressure term was later validated by Zhao and Marshall [5], who also investigated the finger instability phenomenon, induced by surface heterogeneity. Sellier [6] considered the perturbation induced by a 3D obstacle on the one dimensional flow of a film flowing down a vertical plane, focusing on the liquid distribution around the obstacle and the influence of the obstacle shape, rather than on the dry-patch dynamics.

The aim of this paper is the development of an efficient solver for the governing lubrication equation suitable as a first step for the analysis of complex, real world configurations like the one encountered, as an example, in in-flight icing configuration, involving the evolution and interaction of several rivulets, film and dry-patches. Thus, a general, fully implicit, 2D solver is described, commenting on its CPU time efficiency. An upwind discretization is chosen, rather than the central schemes used in [3–8], in order to be able to model also the convection dominated flows where the shear stress is the main driving force (as done, for continuous films, in [9]). The code is first validated with experimental evidences [10, 11] and then applied to the analysis of dry-patch stability dynamics. In particular, the maximum mass flow rate allowing for the growth of a dry-patch is computed from the fully 2D model. Furthermore, the evolution of the contact angle along the whole 2D profile of the patch is presented and commented, while in previous literature references the analysis was limited to the region close to the patch apex.

2. Mathematical model

Consider a thin film of height h flowing along an inclined plane under the action of both gravity and shear. Let α be the inclination of the plane with respect to the horizontal and $\boldsymbol{\tau_a}$ the shear applied by an external gas flow. The continuity equation offers:

$$\frac{\partial h}{\partial t} = -\nabla \cdot \boldsymbol{Q} = -\nabla \cdot (\boldsymbol{u}\, h) \tag{1}$$

For low Reynolds numbers, $\mathrm{Re} \leq 1$, the lubrication theory allows to write the average film velocity as a function of the shear stress and of the gradient of pressure p:

$$\boldsymbol{u} = -\frac{\nabla p}{3\,\mu}\, h^2 + \frac{\boldsymbol{\tau_a}}{2\,\mu}\, h \tag{2}$$

Substituting Eq. (2) in Eq. (1) leads to

$$\frac{\partial h}{\partial t} = -\nabla \cdot \left(-\frac{\nabla p}{3\,\mu}\, h^3 + \frac{\boldsymbol{\tau_a}}{2\,\mu}\, h^2 \right) \tag{3}$$

The pressure field of the liquid is given by Schwartz and Eley [4] as

$$p = \rho\, g \left(h\, \cos\alpha - x\, \sin\alpha \right) - \sigma\, \nabla^2 h - \Pi \tag{4}$$

where

- $\rho\, g\ (h\, \cos\alpha - x\, \sin\alpha)$ represents the contribution of gravity pressure, x increasing in the downhill direction of the plane;
- the capillary pressure $\sigma\, \nabla^2 h$ is due to the curvature of the liquid-gas interface;

- the disjoining pressure Π, related to the intermolecular forces between liquid and solid substrate, is given by

$$\Pi = B\left[\left(\frac{h_{wet}}{h}\right)^n - \left(\frac{h_{wet}}{h}\right)^m\right] \tag{5}$$

  where h_{wet} is the height of the precursor film and the parameters m, n, B have to be defined according to the constraints $1 < m < n$, $B > 0$.

In particular, writing the equilibrium of forces for a liquid volume near the contact line, Schwartz and Eley [4] obtained the following expression of the coefficient B,

$$B = \frac{1}{h_{wet}}\frac{(n-1)(m-1)}{(n-m)}\,\sigma\,(1-\cos\theta_e) \tag{6}$$

where θ_e is the equilibrium contact angle.

Zhao and Marshall [5] demonstrated consistency of Eq. (6), but they observed that values of the precursor film height h_{wet} much larger than the physical one (which is related to the range of intermolecular forces) are usually chosen for numerical simulations, leading to inaccurate results. Hence they introduced the correction factor f,

$$f = 1 + 6.069\left(\frac{h_{wet}}{h_\infty}\right) + 161.7\left(\frac{h_{wet}}{h_\infty}\right)^2 - 1547\left(\frac{h_{wet}}{h_\infty}\right)^3 + 5890\left(\frac{h_{wet}}{h_\infty}\right)^4 \tag{7}$$

which multiplies the coefficient B.

Defining the non-dimensional quantities

$$\bar{h} = \frac{h}{h_\infty}\;;\;\bar{\boldsymbol{x}} = \frac{\boldsymbol{x}}{h_\infty}\;;\;\bar{t} = \frac{t}{(h_\infty/u_\infty)}\;;\;\bar{\tau}_a = \frac{\tau_a}{(\sigma/h_\infty)}\;;\;\bar{p} = \frac{p}{(\sigma/h_\infty)}\;;\;\bar{\Pi} = \frac{\Pi}{(\sigma/h_\infty)} \tag{8}$$

and introducing Bond and Capillary numbers, Eqs. (3) and (4) can be rearranged in non-dimensional form

$$\frac{\partial\bar{h}}{\partial\bar{t}} = -\frac{1}{\mathrm{Ca}}\nabla\cdot\bar{\boldsymbol{Q}} = -\frac{1}{\mathrm{Ca}}\nabla\cdot\left(-\frac{\nabla\bar{p}}{3}\bar{h}^3 + \frac{\bar{\boldsymbol{\tau}}_{\boldsymbol{a}}}{2}\bar{h}^2\right) \tag{9}$$

$$\bar{p} = \mathrm{Bo}\left(\bar{h}\,\cos\alpha - \bar{x}\,\sin\alpha\right) - \nabla^2\bar{h} - \bar{\Pi} \tag{10}$$

The fourth order, non-linear PDEs, Eqs. (9) and (10), are solved numerically on a 2D domain on the inclined plane surface. The special case of gravity and shear acting in the same direction is considered. Thus, the average velocity of the undisturbed film is given by:

$$u_\infty = \frac{\rho\,g\,\sin\alpha}{3\,\mu}\,{h_\infty}^2 + \frac{\tau_a}{2\,\mu}\,h_\infty \tag{11}$$

3. Spatial discretization

The 2D spatial domain $L_x \times L_y$ is discretized using an uniform, orthogonal grid composed by $n_{el} = n_i \times n_j$ elements of dimensions Δx and Δy. The convective term $\nabla\cdot\boldsymbol{Q}$ of Eq. (1) is discretized via a first order upwind scheme. Hence, the flux $\boldsymbol{Q} = \boldsymbol{u}\,h$ is decomposed into two contributions. With reference to x direction, $Qx^+ = u^+\,h$ refers to the the wave propagation with positive velocity, while $Qx^- = u^-\,h$ refers to the wave propagation with negative velocity.

Using finite volume notation and referring to non-dimensional quantities, the volume integral of the divergence for the $i,j-$th element can be expressed as an integral over its boundary surface $\Omega_{i,j}$, with $\hat{\boldsymbol{n}}$ outward unit normal vector:

$$\frac{1}{V_{i,j}}\int_{V_{i,j}}\nabla\cdot\bar{\boldsymbol{Q}} = \frac{1}{V_{i,j}}\int_{\Omega_{i,j}}\bar{\boldsymbol{Q}}\cdot\hat{\boldsymbol{n}}\,d\Omega = \frac{\bar{Q}x_{i+\frac{1}{2},j} - \bar{Q}x_{i-\frac{1}{2},j}}{\Delta\bar{x}} + \frac{\bar{Q}y_{i,j+\frac{1}{2}} - \bar{Q}y_{i,j-\frac{1}{2}}}{\Delta\bar{y}} \tag{12}$$

The fluxes that cross the faces of the $i,j-$th element in the x direction can be calculated as:

$$\bar{Q}x_{i-\frac{1}{2},j} = \frac{1}{2}\left(\bar{Q}x^{+}{}_{i-1,j} + \left|\bar{Q}x^{+}{}_{i-1,j}\right|\right) + \frac{1}{2}\left(\bar{Q}x^{-}{}_{i,j} - \left|\bar{Q}x^{-}{}_{i,j}\right|\right) \tag{13}$$

$$\bar{Q}x^{+}{}_{i,j} = \left(\bar{u}^{+}\,\bar{h}\right)_{i,j} = \left(-\frac{1}{3}\frac{\bar{p}_{i+1,j} - \bar{p}_{i,j}}{\Delta\bar{x}}\,\bar{h}_{i,j}^{2} + \frac{\bar{\tau}_a}{2}\,\bar{h}_{i,j}\right)\bar{h}_{i,j} \tag{14}$$

$$\bar{Q}x^{-}{}_{i,j} = \left(\bar{u}^{-}\,\bar{h}\right)_{i,j} = \left(-\frac{1}{3}\frac{\bar{p}_{i,j} - \bar{p}_{i-1,j}}{\Delta\bar{x}}\,\bar{h}_{i,j}^{2} + \frac{\bar{\tau}_a}{2}\,\bar{h}_{i,j}\right)\bar{h}_{i,j} \tag{15}$$

The expressions of the fluxes $\bar{Q}x^{+}{}_{i,j}$ and $\bar{Q}x^{-}{}_{i,j}$ ensure that the pressure gradient on each face is always computed with a centered difference:

$$\left(\frac{\partial\bar{p}}{\partial\bar{x}}\right)_{i\pm\frac{1}{2},j} = \frac{\bar{p}_{(i\pm\frac{1}{2})+\frac{1}{2},j} - \bar{p}_{(i\pm\frac{1}{2})-\frac{1}{2},j}}{\Delta\bar{x}} \tag{16}$$

The pressure field, Eq. (10), is calculated from the values of the film distribution $\bar{h}$ and substituted in Eqs. (14) and (15). The capillary pressure $\nabla^2\bar{h}$, the only contribution depending on the spatial derivates of $\bar{h}$, is implemented via a centered scheme, leading to

$$\left(\frac{\partial^2\bar{h}}{\partial\bar{x}^2}\right)_{i,j} = \frac{\bar{h}_{i-1,j} + \bar{h}_{i+1,j} - 2\,\bar{h}_{i,j}}{\Delta\bar{x}^2} \tag{17}$$

for the x direction. Combining centered scheme to calculate the capillary pressure and upwind to calculate the fluxes through the element faces, it is easy to demonstrate that the higher order derivates of $\bar{h}$ are treated with a centered scheme.

4. Time discretization

Von Neumann analysis for an explicit Euler discretization of the linearized PDE

$$\frac{\partial\bar{h}}{\partial\bar{t}} = -\frac{1}{3\,\mathrm{Ca}}\,\frac{\partial^4\bar{h}}{\partial\bar{x}^4} \tag{18}$$

gives the following stability constraint for the time step:

$$\Delta\bar{t} \leq \frac{3}{8}\,\mathrm{Ca}\,\Delta\bar{x}^4 \tag{19}$$

Eq. (19) clearly shows that an explicit scheme to solve Eqs. (9) and (10) is computationally too expensive if good resolution ($\Delta\bar{x} < 1$) is required. The same conclusion is reported by several authors [3–5, 12]. Thus, an implicit Euler scheme is chosen. A straightforward implementation would lead to a sparse system of non-linear algebraic equations. However, on the structured grid used in the present work, the computational time can be greatly reduced following an alternate direction implicit (ADI) scheme. Witelski and Bowen [3] considered the numerical resolution of high-order non-linear diffusion equations and suggested to treat explicitely the mixed derivates of $\bar{h}$ when applying the ADI approximate factorization.

Thus the film flux is decomposed into two components isolating the mixed derivates of $\bar{h}$, which derive from the gradient of the capillary pressure, in the expression of $\bar{\boldsymbol{Q}}$:

$$\bar{\boldsymbol{Q}} = \bar{\boldsymbol{F}} + \frac{\bar{h}^3}{3}\left\{\begin{array}{c} \dfrac{\partial}{\partial\bar{x}}\left(\dfrac{\partial^2\bar{h}}{\partial\bar{y}^2}\right) \\ \dfrac{\partial}{\partial\bar{y}}\left(\dfrac{\partial^2\bar{h}}{\partial\bar{x}^2}\right) \end{array}\right\} \tag{20}$$

Linearizing $\bar{\boldsymbol{F}}$ by means of the Jacobian matrix and applying the approximate factorization of [3], the sparse, non-linear system of algebraic equations can be decomposed into two pentadiagonal, linear systems to solve together.

It is worth to point out that only first-order accuracy in time is obtainable from two-step schemes (as Eulero and Crank-Nicolson) when mixed derivates are involved in ADI factorization. The time step $\Delta\bar{t}$ is dinamically adjusted as,

$$\Delta\bar{t} = \frac{\kappa}{\max\left\{\frac{|\bar{h}_{i,j}^{n+1} - \bar{h}_{i,j}^{n}|}{\bar{h}_{i,j}^{n+1}}\right\}} \Delta\bar{t} \tag{21}$$

where κ is maximum allowed increment $\Delta h/h$ (usually $\kappa \leq 0.02$).

5. Boundary and initial conditions

At the inlet boundary ($x = 0$), the undisturbed film flow per unit length $\dot{V} = u_\infty\, h_\infty$ is supposed to enter the domain, giving $\bar{\boldsymbol{Q}}_{\boldsymbol{in}} \cdot \hat{\boldsymbol{n}} = 1$; remembering Eq.(4), this condition implies that the inlet pressure equals the one of the undisturbed film, $\bar{p}_\infty = \mathrm{Bo}\cos\alpha + \bar{\Pi}_\infty$. At the outlet boundary ($x = L_x$), zero flux entering the domain and zero pressure gradient, $\bar{\boldsymbol{Q}}_{\boldsymbol{in}} \cdot \hat{\boldsymbol{n}} = 0$ and $\nabla\bar{p} \cdot \hat{\boldsymbol{n}} = 0$ respectively, are imposed. At the lateral boundaries, simmetry conditions $\bar{\boldsymbol{Q}} \cdot \hat{\boldsymbol{n}} = 0$ and $\nabla\bar{p} \cdot \hat{\boldsymbol{n}} = 0$ are imposed.

The onset of the dry-patch is induced by a discontinuity in the initial wetting properties of the substrate, rather than introducing a physical obstacle as in [6]. In particular, the film flow is iniatialized with a nonwettable small square patch, imposing: zero flux through the nonwettable patch boundaries, $\bar{\boldsymbol{Q}} \cdot \hat{\boldsymbol{n}} = 0$; fixed film height $\bar{h}_{i,j} = \bar{h}_{wet}$ inside the nonwettable patch.

Two sets of different initial conditions can be chosen:

- dry condition $\Rightarrow\ \bar{h}_{i,j} = \begin{cases} 1 \text{ if } x_{i,j} < 0.1\, L_x \\ \frac{h_{wet}}{h_\infty} \text{ if } x_{i,j} > 0.1\, L_x \end{cases}$
- wet condition $\Rightarrow\ \bar{h}_{i,j} = 1$.

The wet condition describes the flow of a film, initially undisturbed, perturbed by the obstacle; the dry condition allows to study the contact line motion and possibly the phenomena related to finger instability.

6. Validation

We validate the code simulating the experimental configurations of [10, 11] and comparing the dry-patch shape with the prediction of the empirical model of Podgorski et al. [10], which validity is confirmed by its perfect agreement with several experimental data [10, 11]. Silicon oil, $\rho = 950\ \left(\mathrm{kg/m^3}\right)$, $\mu = 0.019$ (Pa s) and $\sigma = 0.021$ (N/m), and equilibrium contact angle equal to $\theta_e = 20^\circ$ are chosen for the following simulations.

Starting from an undisturbed film flow on the inclined plane, we apply the nonwettable small patch defined in the previous paragraph in order to perturb the flow and eventually generate a dry-patch. The choice of the obstacle size L_o follows Sellier [6]:

$$\frac{L_o}{h_\infty} = (\mathrm{Bo}\sin\alpha)^{-\frac{1}{3}} \tag{22}$$

Each computation is identified by the inclination α of the plane with respect to the horizontal, the magnitude of the shear τ_a and the undisturbed film flow per unit length $\dot{V}$; τ_a is set to zero for the following simulations. Grid independence analysis suggested the use of a non-dimensional spatial discretization step in the range $[0.025 - 1]$, and the precursor film heigth h_{wet} is set at

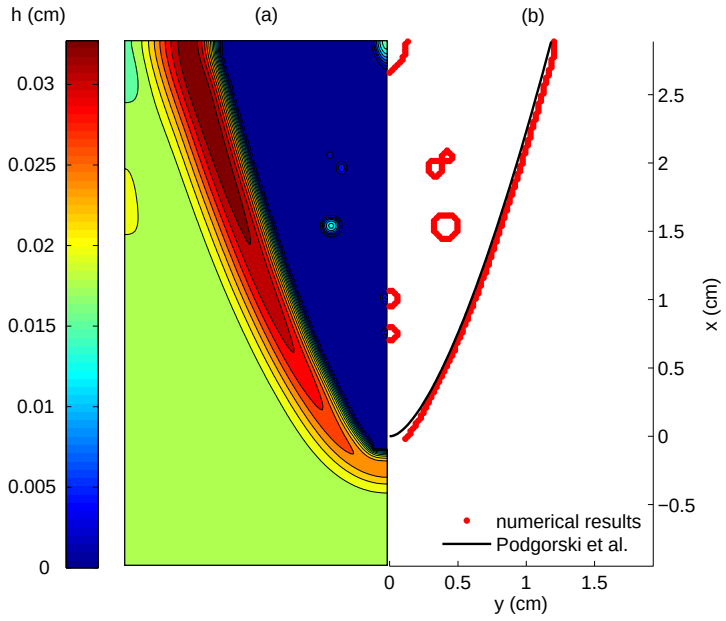

Figure 1. Computed film height (a); dry-patch validation (b). $\dot{V} = 5.9 \times 10^{-3}\,\mathrm{cm}^2/\mathrm{s}$, $\alpha = 30°$.

5% of h_∞, following [4, 5]. The choice of disjoning pressure parameters $(m,\, n) = (2,\, 3)$ is driven by stability considerations [4, 5].

The numerical result of figure 1(a) shows the stationary distribution $h(x, y)$ of the film height. Confirming both experimental and analytical evidences [10, 11, 13], a capillary ridge with higher film thickness and flow rate appears near the contact line of the resulting dry-patch. Moreover, some residual drops, that are slowly draining, can be observed. Figure 1(b) compares numerical results with the dry-patch model given in [10]: it can be noticed that the numerical dry-patch fits exactly the empirical model.

7. Results and discussion

The implicit code was applied to the dry-patch stability analysis, estimating the maximum critical mass flow allowing for its persistence. Following the procedure of experimental tests in [10], the undisturbed flow is first perturbed in order to generate a dry-patch, as in the previous paragraph. Once the stationary condition is reached, the obstacle is removed: if the dry-patch is stable (i.e. the contact line doesn't move and a new stationary condition is immediatly reached) the imposed flow rate $\dot{V}$ is lower then the critical one; if the contact line starts advancing or the dry-patch closes up, $\dot{V}$ is higher than $\dot{V}_{cr}$.

Running the code for increasing value of the film flow rate until the critical condition is reached, a set of points describing the critical flow rate dependence on the inclination of the plane was obtained. This allowed us to compare the numerical results with an empirical model, which simplifies the determination of the critical flow rate. This model derives from the assumption that a capillary ridge, where the liquid flows along the contact line direction, surrounds the dry-patch. Following [10, 14], mass, momentum and energy balances are written for the ridge volume

surrounding the dry-patch apex. Following the procedure described in detail in [14] we obtain:

$$1 - \cos\theta_e = \mathrm{We} + \mathrm{Bo}\left(\cos\alpha + \frac{S_r}{{h_\infty}^2}\,\sin\alpha\right) \tag{23}$$

$$\frac{p}{(\sigma/h_\infty)} = \frac{\mathrm{We}}{2} + \mathrm{Bo}\left(\cos\alpha + \frac{1}{2}\,\frac{L_r}{h_\infty}\,\sin\alpha\right) \tag{24}$$

where S_r and L_r are the ridge transverse section area and the ridge width, normal to the contact line, respectively. The mean pressure inside the ridge is given by the capillary pressure:

$$p = -\frac{1}{L_r}\int_0^{L_r}\sigma\,\frac{d^2h}{dl^2}\,dl = -\frac{\sigma}{L_r}\left[\frac{dh}{dl}\right]_0^{L_r} = \frac{\sigma}{L_r}\Big[\tan\Theta\Big]_0^{\theta_e} = \sigma\,\frac{\tan\theta_e}{L_r} \tag{25}$$

Introducing the non-dimensional parameter $\gamma = L_r\,h_\infty/S_r$ in order to describe the ridge shape, calculating Weber number and Bond number with respect to the inlet film flow rate $\dot{V} = u_\infty\,h_\infty$, the critical flow rate $\dot{V}_{cr}$ can be calculated solving Eqs. (23), (24) and (25). Figure 2 shows

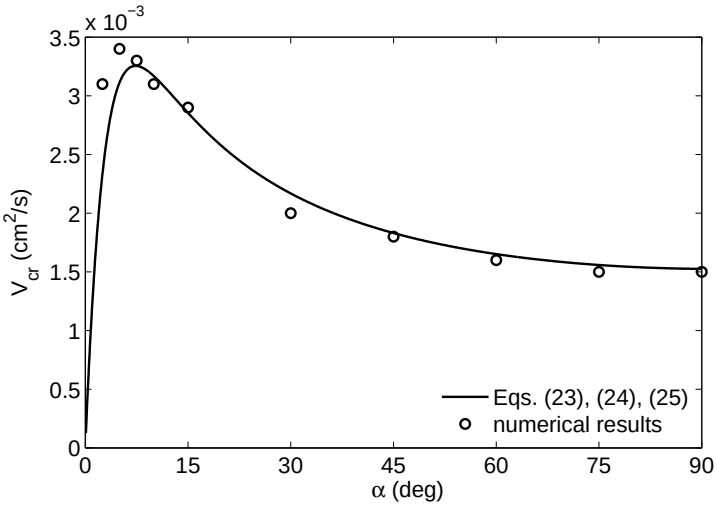

Figure 2. Critical flow rate for $\theta_e = 20°$.

the critical flow rate as a function of the plane inclination for $\theta_e = 20°$ deriving from numerical simulations (circles), fitted by the simplified model (continuous line). The empirical model described above best fits the numerical results when $\gamma = 0.921$.

The dynamics of dry-patch re-wetting was also studied: if the imposed flow rate exceeds the critical value the dry-patch is unstable and will be someway shed away once the nonwettable patch is removed. Figure 3(a) shows the dry-patch contact line at different time step for a high value of the film flow rate, $\dot{V} >> \dot{V}_{cr}$. The dry-patch first adjusts its shape after the obstacle removal and then advances with a constant velocity, due to gravity force, rather than closing up. In figure 3(b) the position of dry-patch apex is traced as a function of time, confirming that a characteristic draining velocity, lower then the undisturbed film velocity u_∞, is reached. From other simulations, which results are not shown due to space limitation, it was observed that, when the flow rate is close to the critical value, $\dot{V} \simeq \dot{V}_{cr}$, a characteristic draining velocity is still reached, confirming the dry-patch motion along the inclined plane, but the dry-patch also tends to close up with a lower velocity, perpendicular to the contact line itself, due to capillary effect.

Finally, the consistence of the disjoining pressure model for describing the dynamics near the contact line is also analyzed. The value of the equilibrium θ_e, in fact, is used to define the

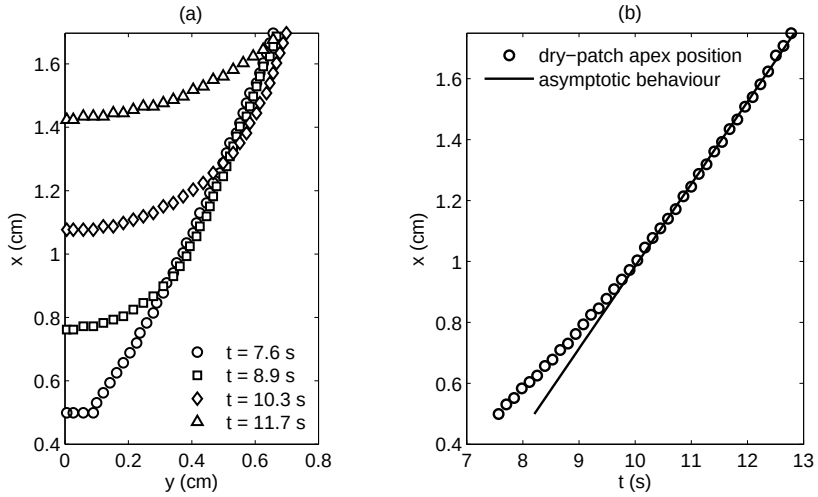

Figure 3. Contact line at different time (a); dry-patch apex position as a function of time (b). $\dot{V} = 7.5 \times 10^{-3}\,\mathrm{cm}^2/\mathrm{s}$, $\alpha = 30°$.

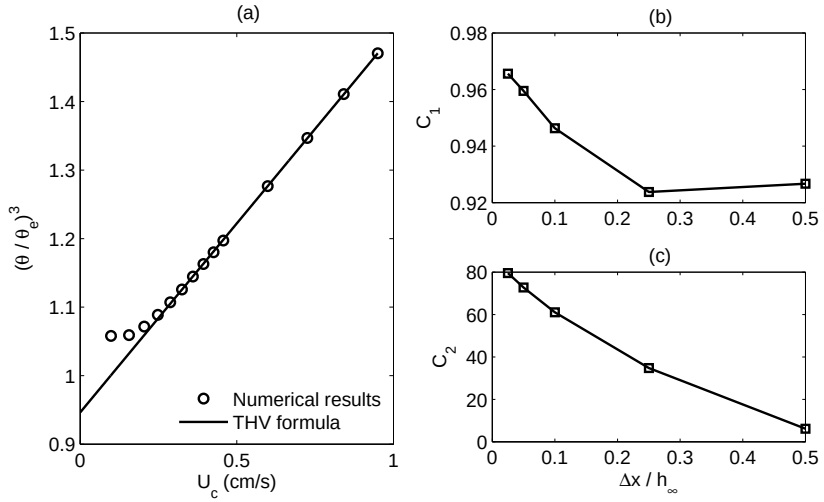

Figure 4. Dynamic contact angle for 1D film flow as a function of contact line velocity, $\Delta x = 0.1\,h_\infty$ (a); influence of discretization accuracy on regression coefficients of Eq.(26) (b).

disjoining pressure from Eq. (6). However, the actual θ is calculated from the slope of the film thickness distribution at the contact line, i.e. from the local modulus of the gradient of h. Zhao and Marshall [5] validated Eqs. (5) and (6) in the case of one dimensional film flow advancing along an inclined plane, concluding that the calculated dynamic contact angle respects the modified Tanner−Hoffman−Voinov formula,

$$\theta^3 = \theta_e^3 \left(C_1 + C_2 \frac{\mu\, u_c}{\sigma} \right) \; ; \; \frac{u_c}{u_\infty} = \frac{1 - (h_{wet}/h_\infty)^3}{1 - (h_{wet}/h_\infty)} \tag{26}$$

where θ and θ_e are the dynamic and static contact angles respectively, u_c is the contact line velocity, which depends on the undisturbed film velocity and the precursor film thickness, and C_1, C_2 are constants (C_1 depending on the spatial discretization accuracy, which influences the calculated value of θ).

Simulations were run considering the 1D problem (a film flowing over an inclined plane initially dry) with $\theta_e = 20°$ and $\alpha = 30°$. Figure 4(a) shows the dynamic contact angle as a function of the contact line velocity u_c: the 1D numerical results (circles) are fitted by Eq. (26); in order to guarantee a good resolution near the contact line, it was chosen a spatial discretization step equal to $\Delta x/h_\infty = 0.1$. The effect of a change in the spatial discretization accuracy on the evaluation of θ is shown in figure 4(b). It can be noticed that the regression coefficient C_1 of Eq. (26) tends to 1 (i.e. the condition $\theta = \theta_e$ if $u_c = 0$ is respected) for high discretization accuracy ($\Delta x \to 0$).

The dynamic contact angle is also studyed in the 2D case: a dry-patch is generated perturbing the undisturbed flow by an obstacle, which is then removed allowing for the contact line movement. Simulations were run for different values of the imposed flow rate $\dot{V}$: a moving dry-

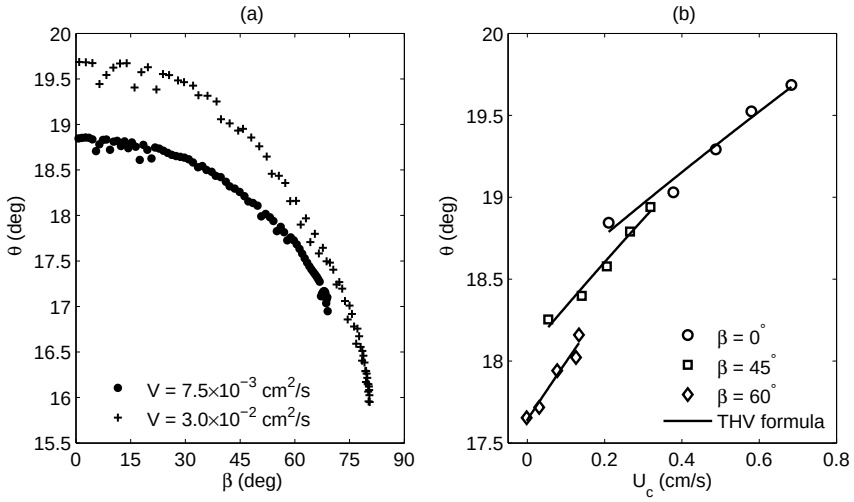

Figure 5. Dynamic contact angle as a function of the contact line inclination for two different flow rates (a); dependence of the contact angle on contact line velocity, for $\dot{V} = 0.75, 1.5, 2.0, 3.0 \times 10^{-2}\,\mathrm{cm}^2/\mathrm{s}$ (b).

patch is captured and the contact angle calculated. Figure 5(a) demonstrates that the dynamic contact angle strongly depends on the position, here identified by the angle β between the normal to the contact line and the x direction ($\beta = 0$ at the patch apex). The contact angle θ decreases for increasing value of β. This trend is confirmed by the relation $\tan\theta \propto x^{-\frac{3}{4}}$, obtained via post-processing of the results of [13], where the authors solved analitically a simplified version of Eqs. (3) and (4). Two different shapes of θ as a function of β, see figure 5(a), were obtained for two different flow rates: the discrepancy between the two curves is due to the additional dependence of θ from the contact line velocity. In figure 5(b) three values of β are chosen and the contact angle θ is plotted, for each β, against the contact line velocity, showing that Eq. (26) is still valid. The contact line velocity is calculated numerically, tracing shape and position of the contact line when marching in time, under the assumption that it always moves along its normal direction.

Comparing the performances of the implicit code with the explicit one on the same test case of figure 1 reveals a gain of about $10^2 - 10^3$ on Δt and a corresponding strong reduction in terms of simulation time, of the order of 10^{-2}. Moreover, time step of about 10^6 the Neumann limit, Eq. (19), are reached running the ADI code with spatial discretization step of about h_{wet}.

8. Conclusion

An implicit code was implemented in order to predict the distribution of a gravity driven film over an inclined plane under the assumpions typical of lubrication theory. The code was first validated generating a dry-patch by the implementation of an obstacle and comparing its shape with the one predicted by a literature empirical model of Podgorski et al. [10].

The dry-patch stability analysis allowed to define a critical flow rate, above which the dry-patch moves under the action of gravity. Such threshold value is of obvious importance for a number of practical implementations including heat transfer and film flows. As confirmed also by experimental evidences [10, 11], the model of Hartley and Murgatroyd [1] is not able to predict whenever a dry-patch is stable or not. A novel symplified model for the critical mass flow rate, useful as a quick and easy global threshold value for practical applications, was thus described and validated against numerical predictions.

Once the disjoining pressure model for describing the surface wettability had been validated for a 1D film flow, the dynamic contact angle along the contact line of a moving dry-patch was analyzed: the contact angle decreases when the liquid flows along the contact line tangential direction, in agreement with previous analytical evidences.

The model allows for the analysis of shear driven film and the numerical solution of lubrication equations can be applied to more complex problems, including multiple dry-patch generation, dynamics of drops growth and coalescence or problems involving condensation and evaporation. Moreover, practical problems, such as in-flight icing phenomena or fogging and defogging simulations on car windshield, involve complex geometries, which may require unstructured grids for an easier description of the physical domain. However, even in the present structured grid form, the code may provide a useful insight on the physical mechanisms driving the evolution of a discontinuous film, as well as important quantitative indication on proper threshold values for possible film breakups and transitions.

Nomenclature

B	disjoining coefficient ($\mathrm{N\,m^{-2}}$)
$C_{1,2}$	THV formula coefficients
g	acceleration of gravity ($\mathrm{m\,s^{-2}}$)
h	film thickness (m)
L	length (m)
m, n	disjoining exponents
p	pressure ($\mathrm{N\,m^{-2}}$)
$\boldsymbol{Q}$	mass flow per unit length ($\mathrm{m^2\,s^{-1}}$)
S	section area ($\mathrm{m^2}$)
t	time (s)
$\boldsymbol{u}$	flow velocity vector ($\mathrm{m\,s^{-1}}$)
$\dot{V}$	undisturbed film flow rate ($\mathrm{m^2\,s^{-1}}$)
x, y	Cartesian coordinates (m)

Greek symbols:

α	inclination of the plate (deg)
β	angle between the normal to the contact line and the plate downhill direction (deg)
γ	aspect ratio
θ	contact angle (deg)
μ	dynamic viscosity (Pa s)
Π	disjoining pressure ($\mathrm{N\,m^{-2}}$)
ρ	density ($\mathrm{kg\,m^{-3}}$)
σ	surface tension ($\mathrm{N\,m^{-1}}$)
$\boldsymbol{\tau}$	shear stress ($\mathrm{N\,m^{-2}}$)

Dimensionless numbers:

$\mathrm{Bo} = \rho\, g\, {h_\infty}^2/\sigma$	Bond number
$\mathrm{Ca} = \mu\, u_\infty/\sigma$	Capillary number
$\mathrm{Re} = \rho\, u_\infty\, h_\infty/\mu$	Reynolds number
$\mathrm{We} = \rho\, {u_\infty}^2\, h_\infty/\sigma$	Weber number

Subscripts and superscripts:

$^-$	dimensionless
∞	undisturbed film
a	external gas flow
cr	critic
e	equilibrium
i, j	number of the grid element
n	number of the time step
o	obstacle
r	capillary ridge
wet	precursor film

References

[1] Hartley D E and Murgatroyd W 1964 *Int Journal of Heat and Mass Transfer* **7** 1003
[2] De Candido E, Croce G and D'Agaro P 2012 *Heat Transfer Engineering* **33**(13) 1130
[3] Witelski T P and Bowen M 2003 *Applied Numerical Mahtematics* **45** 331
[4] Schwartz L W and Eley R R 1998 *Journal of Colloid and Interface Science* **202** 173
[5] Zhao Y and Marshall J S 2006 *Journal of Fluid Mechanics* **559** 355
[6] Sellier M 2015 *Int Journal of Multiphase Flow* **71** 66
[7] Weidner D E, Schwartz L W and Eres M H 1997 *Journal of Colloid and Interface Science* **187** 243
[8] Mata M R and Bertozzi A L 2011 *Journal of Computational Physics* **230** 6334
[9] Bourgault Y, Habashi W G, Dompierre J and Baruzzi G S *International Journal for Numerical Methods in Fluids* **29** 429
[10] Podgorski T, Flesselles J M and Limat L 1999 *Physics of Fluids* **11** 845
[11] Rio E and Limat L 2006 *Physics of Fluids* **18** 032102
[12] Diez J A and Kondic L 2002 *Journal of Computational Physics* **183** 274
[13] Wilson S K, Duffy B R and Davis S H 2001 *Euro Journal of Applied Mathematics* **12** 233
[14] Suzzi N, Croce G and D'Agaro P 2015 *Journal of Physics: Conference Series* **655** 012041